Electronic Supplementary Information for:

Lattice Strain Causes Non-Radiative Losses in Halide Perovskites

Timothy W. Jones[#1], Anna Osherov[#2], Mejd Alsari[#3], Melany Sponseller[2], Benjamin C. Duck[1], Young-Kwang Jung[4], Charles Settens[2], Farnaz Niroui[2], Roberto Brenes[2], Camelia V. Stan[6], Yao Li[6,7], Mojtaba Abdi-Jalebi[3], Nobumichi Tamura[6], J. Emyr Macdonald[8], Manfred Burghammer[9], Richard H. Friend[3], Vladimir Bulović[2], Aron Walsh[4,5], Gregory J. Wilson[1], Samuele Lilliu[10,11], and Samuel D. Stranks[*2,3]

*sds65@cam.ac.uk

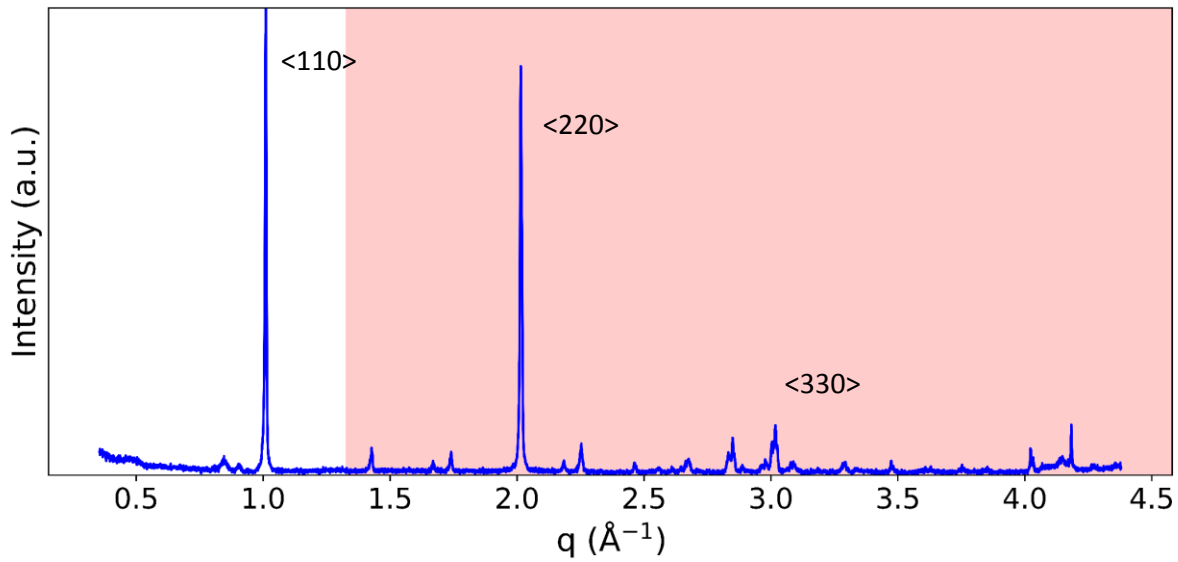

Figure S1. Lab-based X-Ray diffraction pattern. XRD pattern of the $MAPbI_3$ film investigated in this work, with the dominant reflections labelled. The pattern indicates that the <110> planes have preferential orientation. The <110>, <220> and <330> reflections have high intensity values at q = 1, 2 and 3 Å^{-1}, respectively. If we compare the relative intensities of the oriented $MAPI_3$ films to a simulation of randomly oriented tetragonal $MAPI_3$ model (I4cm, Space Group 108), the enhancement in intensity of peaks in <110> is a clear indication of preferred orientation. The shaded region corresponds to the *q* range collected in the μXRD set up.

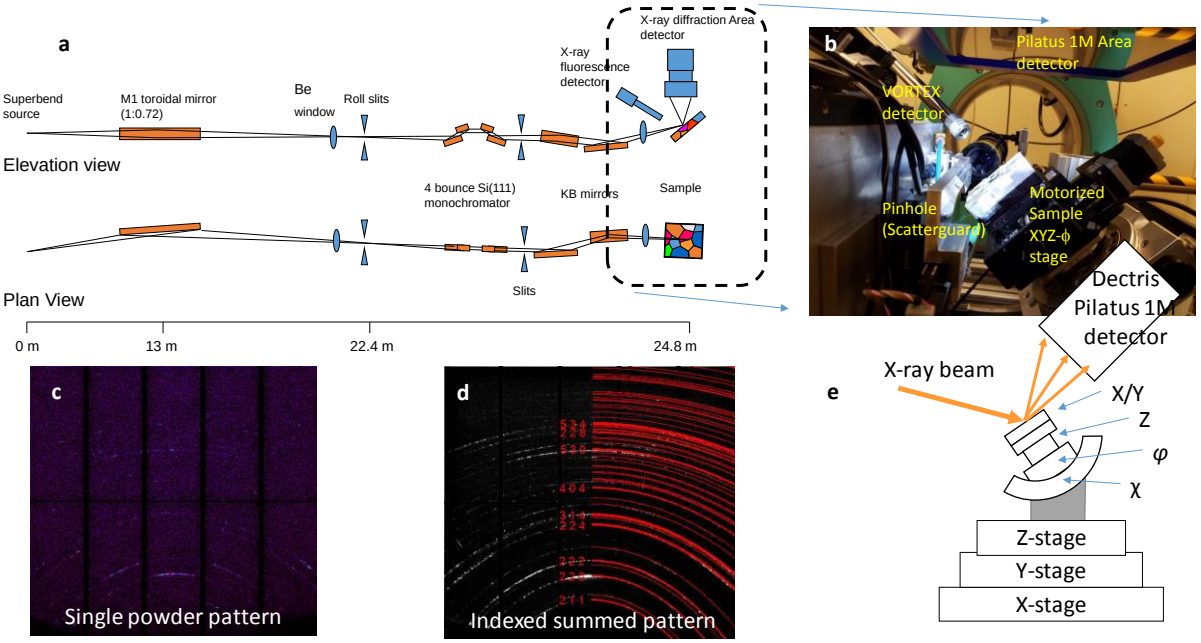

Figure S2. Schematic of the Advanced Light Source X-ray Microdiffraction Beamline 12.3.2 and representative raw data. **(a)** Schematic of beamline optics and end-station, **(b)** Annotated photograph and **(e)** Block schematic of the scanning micro-XRD end station and Cryostream. **(c)** Raw single powder pattern and **(d)** Summed powder patterns across the entire map indexed to $MAPbI_3$. See Video S1 for a movie showing the single powder patterns stepping through different spatial pixels.

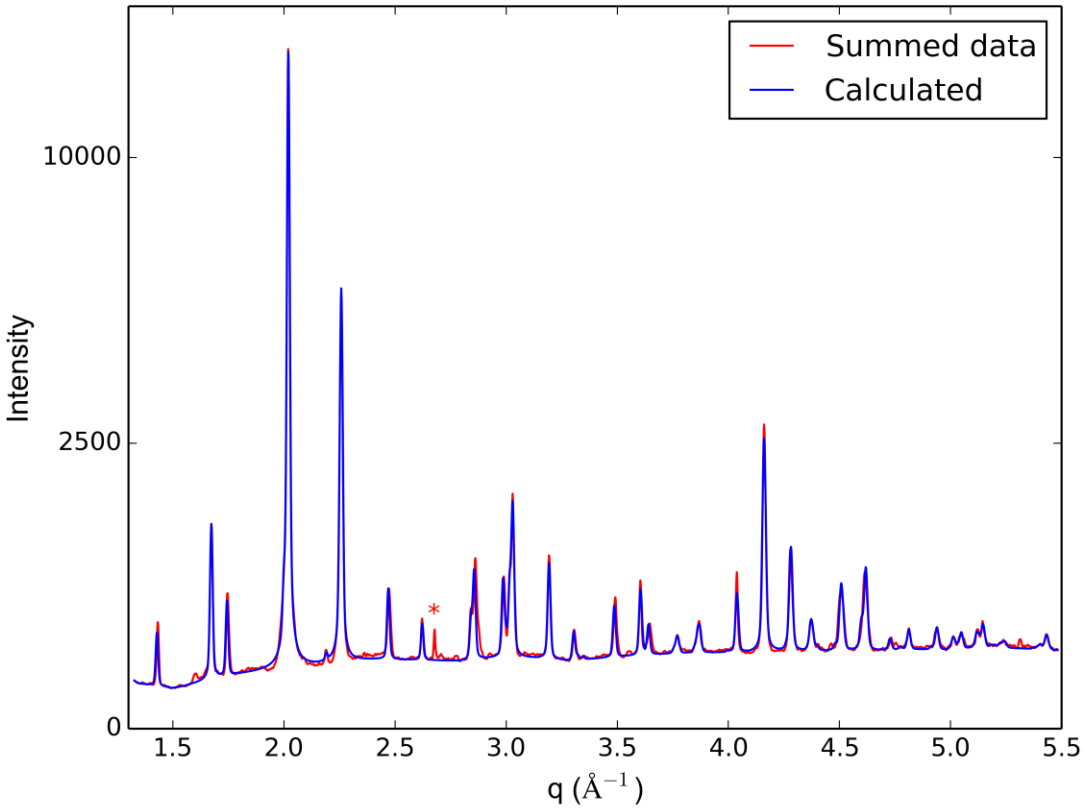

Figure S3. Scanning X-ray microdiffraction pattern of the $MAPbI_3$ thin film constructed by summing each pixel across the entire map. The pattern is indexed to tetragonal $MAPbI_3$. Note the square-root scale of the intensity axis, further emphasizing the low level of beam damage during the scan. The peak marked with a * corresponds to the <111> of the Au platelets [1].

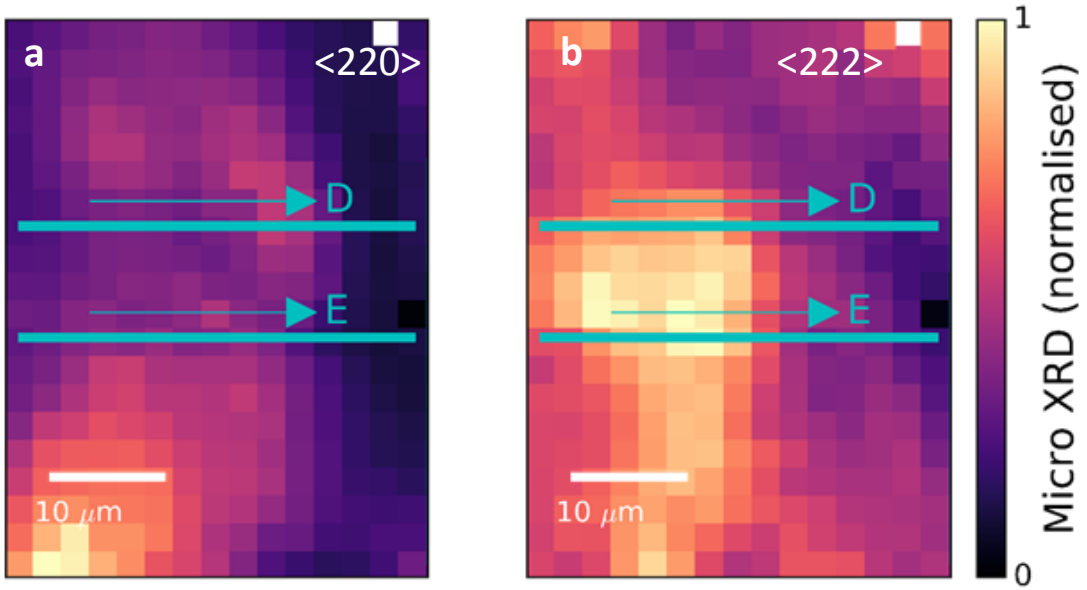

Figure S4. Scanning X-ray microdiffraction peak intensity maps for the <220> and <222>, given at the same location as Figure 1b and c.

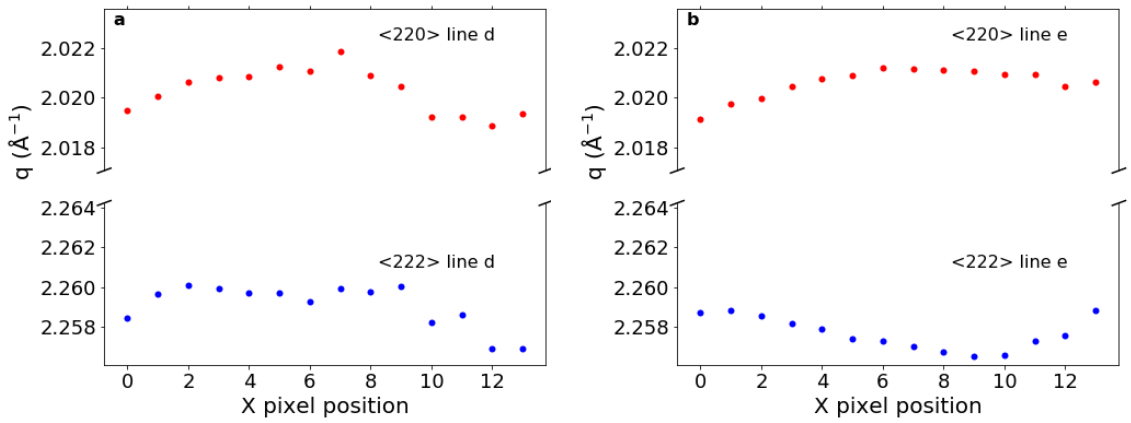

Figure S5. Local variations in <220> and <222> scattering vector *q* from the line profiles of Fig. 1b and c highlighting complex local structure variations on the microscale. **(a)** Line profile d, **(b)** Line profile e.

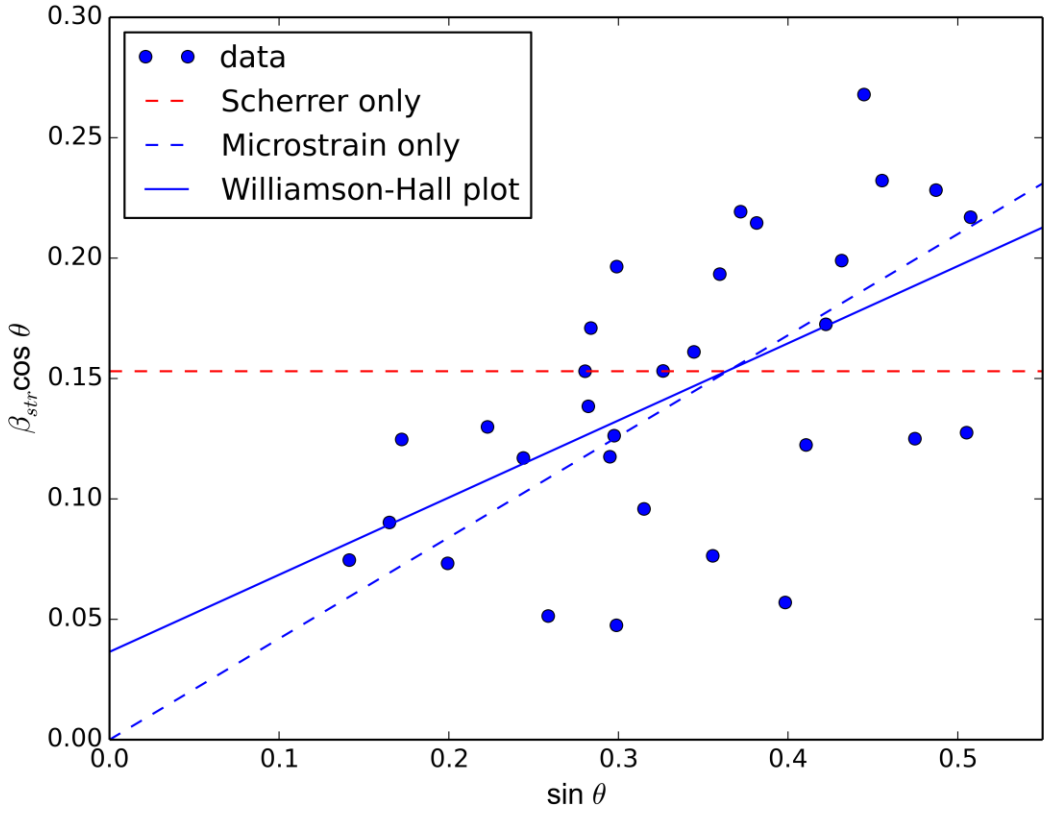

Figure S6. Linear Williamson – Hall Plot of the XRD data from Figure S3. The solid line assumes crystallite size and microstrain; – the dashed line assumes Scherrer crystallite size broadening only; the dotted line assumes microstrain only. Assuming both crystallite size and microstrain, the slope of the linear regression indicates a microstrain of 0.14 ± 0.04 %. Although the intercept of the line is 0.0365, corresponding to a crystallite size value of approximately 200 nm, the variance is 90 nm, and therefore unreliable. The broadening is dominated by microstrain and so assuming a model to neglect the crystallite size term gives a value of microstrain of 0.18 ± 0.01 %. We also find similar results for data from each spatial pixel, which were used to generate the microstrain maps. Note, the β_{str} is in units of degrees.

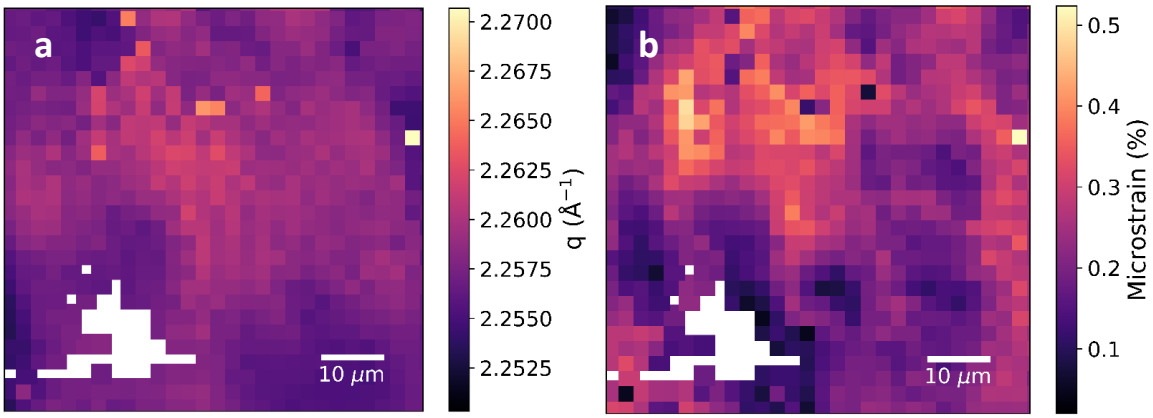

Figure S7. Spatial variations in <222> lattice plane across a $MAPbI_3$ thin film. (a) Map of *q*, (b) Map of microstrain. We note that this map may have intensity contributions from other reflections including <114> and <310> due to peak overlap. This is not the case for the <220>, which is a strongly preferred orientation of the film (cf. Figures S1 and S3). We note that white regions correspond to pixels where insufficient peak intensity was available to reliably fit the line profile, and so are excluded from the map.

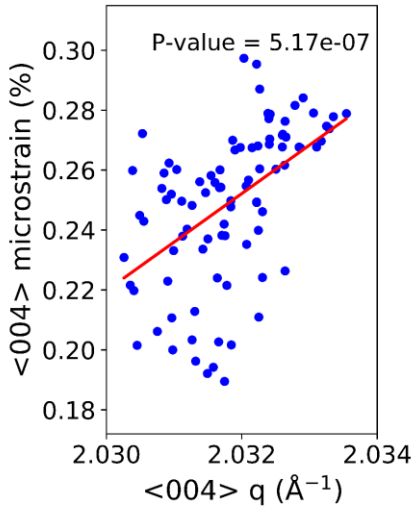

Figure S8. Microstrain-strain relationship extracted from the <004> reflection of the 'triple cation' $MA_{0.15}FA_{0.79}Cs_{0.06}Pb(I_{0.85}Br_{0.15})_3$ perovskite thin film. The μXRD data was measured at ALS in the same manner as for $MAPbI_3$ thin films and analyzed assuming $MAPbI_3$ crystallographic model for simplicity. We note that further analysis would require a more rigorous modeling of the cation occupancy for the alloyed configurations but this will be the subject of future work. Nevertheless, this would not change the nature of the microstrain versus q correlation shown in the figure.

Extraction of microstrain from μ-XRD measurements

Both crystallite size and microstrain (lattice strain) were considered when modelling the broadening of integrated diffraction profiles from the two-dimensional diffraction patterns obtained at ALS Beamline 12.3.2. The analysis was performed on the chi-integrated data extracted from the beamline (XMAS) using the Williamson – Hall method[2] that is available in Panalytical Highscore Plus v4.7 software. We note that the broadening associated with microstrain in the Williamson – Hall formalism may also have contributions from paracrystallinity effects [3].

Quantitative analysis of the μXRD data to extract crystallographic information was performed using tetragonal methyammonium lead iodide (ICSD-250739) with the assumption of preferred orientation in the <110> direction fitted using March-Dollase model [4]. $MAPI_3$ thin film XRD data was refined in an automated matter after fitting to a corundum diffraction pattern to subtract instrumentation-dependent contributions such as zero shift, specimen displacement and correction of intensity based on beam footprint for a 15 degree fixed angle of incidence.

A corundum calibration sample diffraction pattern was collected and the instrumental contribution of the line broadening was first fitted to a Cagliotti equation,

$$\beta_{inst}{}^2 = W + Vtan(\theta) + Utan^2(\theta)$$

where the coefficients *W*, *V*, and *U* are fittable parameters that are instrument specific. The Cagliotti equation allows an analytical form to describe the breadth versus diffraction angle so that if the diffraction angles for the specimen do not match the diffraction angles of the calibrant, the breadths may still be subtracted. A pseudo-Voigt (convolution of a Lorentzian and Gaussian distribution) intensity profile function was used to fit the corundum XRD pattern

to obtain β_{inst} . The Lorentzian and Gaussian contributions of the instrumental breadth were deconvolved and then subtracted from the observed breadth of the diffraction lines from the $MAPI_3$ specimen as follows,

$$\beta_{str} = \sqrt{{\beta_{obs}}^2 - {\beta_{inst}}^2}, \text{ for Gaussian and microstrain dominating,}$$

$$\beta_{str} = \beta_{obs} - \beta_{inst}, \text{ Lorentzian and crystallite size dominating,}$$

where β_{obs} is observed breadth before subtraction, and the remaining breadth after subtraction is renamed, structural breadth, β_{str}.

Internal lattice strains in crystalline grains cause shift of the angular position and shapes of diffraction peaks. If the specimen is compressively strained in a uniform manner (i.e. isotropic) the lattice parameters for all peaks will shift to higher angular position, but the peak will remain sharp. The shift of each peak, $\Delta\theta_B$ caused by a strain, $\varepsilon = \Delta d/d$ is calculated by differentiating Bragg's law.

$$\frac{\mathrm{d}}{\mathrm{d}d} 2dsin(\theta_B) = \frac{\mathrm{d}}{\mathrm{d}d}\lambda$$

$$2sin(\theta_B) + 2dcos(\theta_B)\frac{\mathrm{d}\theta_B}{\mathrm{d}d} = 0,$$

$$\Delta\theta_B = -\varepsilon\, tan(\theta_B)$$

The crystallite size contribution to β_{str} is analysed by the Scherrer equation. Crystallite size and microstrain are interpreted with two analytical terms,

$$\beta_{str}(\Delta\theta) = \overbrace{\frac{k\lambda}{Lcos(\theta)}}^{crystallite\ size} + \overbrace{4\varepsilon tan(\theta)}^{microstrain}$$

The two contributions can be separated by plotting β_{str} cosθ on the ordinate and sinθ on the abscissa. This allows a linear equation to be realized,

$$\overbrace{cos(\theta)\beta_{str}(\Delta\theta)}^{y} = \overbrace{\frac{k\lambda}{L}}^{intercept} + \overbrace{4\varepsilon}^{slope}\overbrace{[sin(\theta)]}^{x}$$

where the microstrain contribution is indicated by the slope/4 and the crystallite size contribution is interpreted based on the y-intercept. The Williamson – Hall method is an estimation technique that indicates the broadening contribution and quantifies the microstrain as a percentage, and the crystallite size value in Å.

To discern the information from the Williamson – Hall method, we found which term dominates the structural broadening. If the microstrain term dominates, the Williamson – Hall plot will show a more sloped best-fit line with an intercept close to zero. If the crystallite size dominates, the best-fit line will have a slope that is approximately zero and the intercept will indicate the average crystallite size. The variance in crystallite size from the Scherrer equation or the microstrain equation will also indicate the dominating factor. If the variance is large the broadening is anisotropic and special considerations must be made to select crystallographic directions that will indicate the average size while mitigating the morphological effects. From these analyses, we found that microstrain was dominating the broadening (Figure S6), which is consistent with the literature [5, 6].

Image registration for μXRD measurements.

In order to correlate the same scan area between different experiments, we used a combination of Au particles and macroscopic scratches as fiducial markers and waymarkers for sharp registration and a combination of optical images, SEM images, PL maps, μXRD maps and μXRF (X-Ray Fluorescence) Maps. An example of a PL map over the region in the SEM image in the inset is shown in Figure S9.

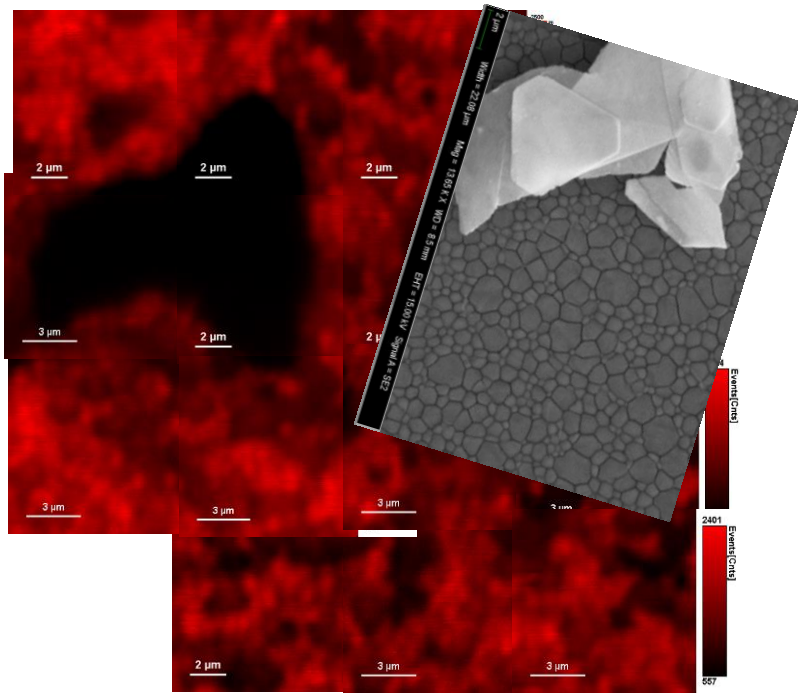

Figure S9. Uniquely-shaped Au particle markers for confocal photoluminescence microscopy and scanning μXRD to obtain correlations in this study. A stitched confocal PL image shows a shadow from Au nanoparticle agglomerates, which attenuated the laser excitation. The agglomerates are shown clearly in the corresponding SEM image.

We summarize our iterative alignment and registration approach in the schematic in Figure S10. As a basis for the images we begin with an optical microscopy image of the samples. Because this image is taken over a larger area than any of the other measurements it is able to function as a base for the following analysis and also contains important identifying features useful for aligning the subsequent data. Secondly an SEM taken of the same region (after μXRD and PL measurement) is aligned to the microscopy image using key features in both images. This SEM image provides scale information to the underlying optical image.

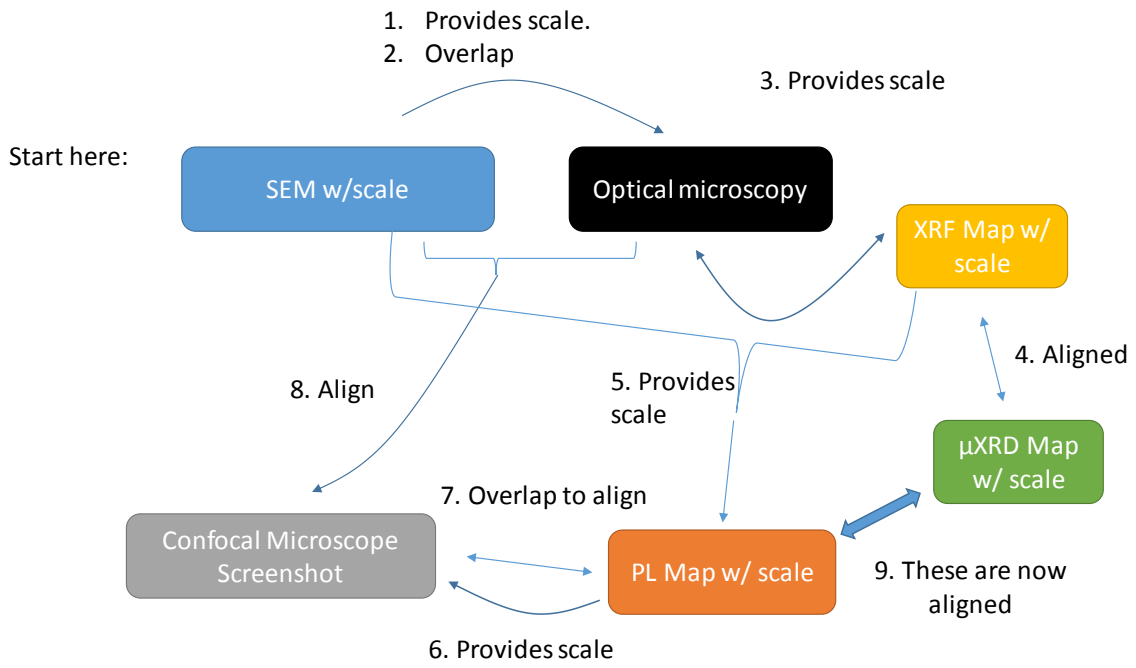

Figure S10. Iterative approach to overlap µXRD and PL data for correlation

Using the scale from the SEM we can now appropriately size the image of the XRD and XRF data. Since the XRD and XRF are taken simultaneously on the same instrument the same coordinate system applies to both. Using the XRF data we can match regions showing reduced material to the area in the optical image that has had the perovskite film removed via fine scratches.

The scale of the SEM and XRD images is used to appropriately size the PL image. An optical image taken on the same system as the PL image is used to correctly position the PL image. Firstly, this second optical image is scaled using identifying features in the PL image. Once correctly scaled, this second optical image is then positioned to overlay the first and allow the correct position and orientation of the PL image to be obtained.

The overlap region of the PL and XRD images can now be identified. The rotation between the two regions has been identified as 2°. To correlate the two datasets we first apply this rotation to the high resolution PL data. The rotated data then undergoes the blurring and

sub sampling procedures to achieve an image with the same characteristics as the XRD (see below for details).

Correlating PL and μ-XRD experiments on the same scan area

In order to correctly assess the correlation between the PL and μXRD images we need to first evaluate both on similar length scales. The much higher resolution of the PL imaging system and the properties of the beam and sample mounting in the micro XRD system mean that the XRD data is sampled over a much larger region. To make our comparison we have applied a blurring procedure to the PL data to simulate the PL observed from an area matching that measured with the XRD system at each point.

The XRD beam profile is described by a Lorentzian profile [7]. In one dimension the Lorentzian profile is given by:

$$I(x) = \left(\frac{\Gamma}{2}\right)^2 \frac{I_{max}}{\left(\frac{\Gamma}{2}\right)^2 + \left(2x + 2x_{peak}\right)^2}$$

where I_{max} is the peak value of the Lorentzian, Γ is the full width half maximum and x_{peak} is the position of the peak value.

We can construct a two dimensional representation of the Lorentzian beam profile by treating the radial distance from the centre of the Lorentzian as the value for *x* in the above equation. This assumes a symmetrical beam profile incident onto the sample and results in an intensity distribution as shown in Figure S11a.

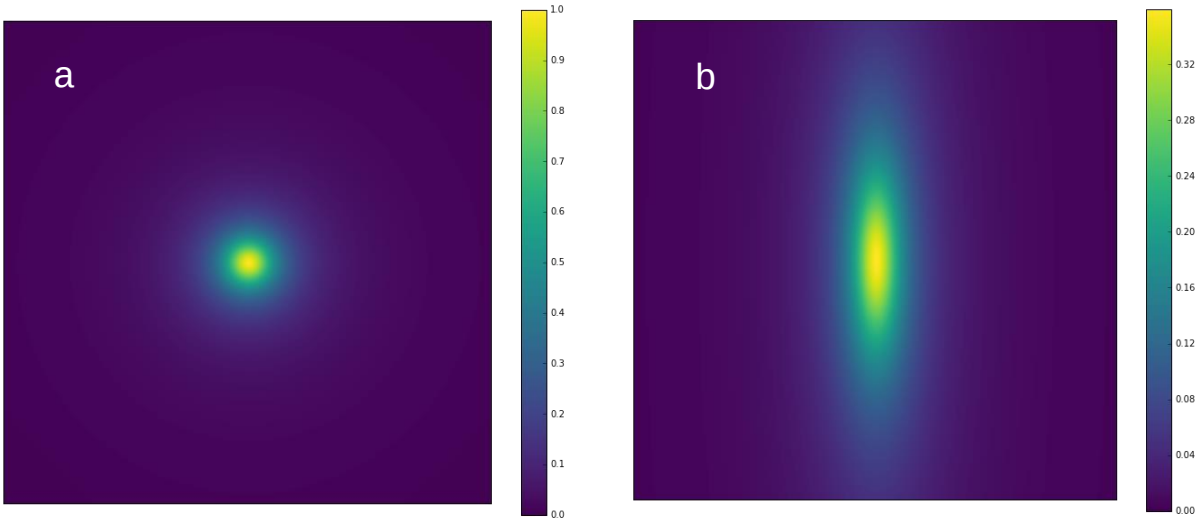

Figure S11. Focused X-ray beam profile projected onto a surface. (a) Surface at normal to beam and (b) beam intensity spread in the y-direction due to the 15 degrees grazing incidence of the sample relative to the beam. Intensities are arbitrary.

Our sample is tilted at an angle of 15° in the y direction. We therefore need to transform the this intensity distribution. This transformation is accomplished by using

$$I(x, y) = I(x, y * \cos(\theta))$$

where θ is the angle of incidence of the beam onto the sample (90° would be normal to the sample surface). Renormalization of the intensity distribution for visualization purposes is accomplished using the ratio of the integrals of the original and transformed intensity data (Figure S11b). This normalization is not precise due to the limits imposed on integrating the Lorentzian distribution however as it is only used for visualization and does not impact the following blurring application we have taken the simplest approach.

Now that we have an intensity distribution, we can treat this as a point spread function and use this to produce a blurred photoluminescence image. A 2D Fourier transform is applied to both the photoluminescence (Figure S12a) and intensity distribution (Figure S11b) data. These are

then combined via pointwise multiplication and an inverse Fourier transform applied to obtain the blurred image. The results of this are shown in Figure S12b.

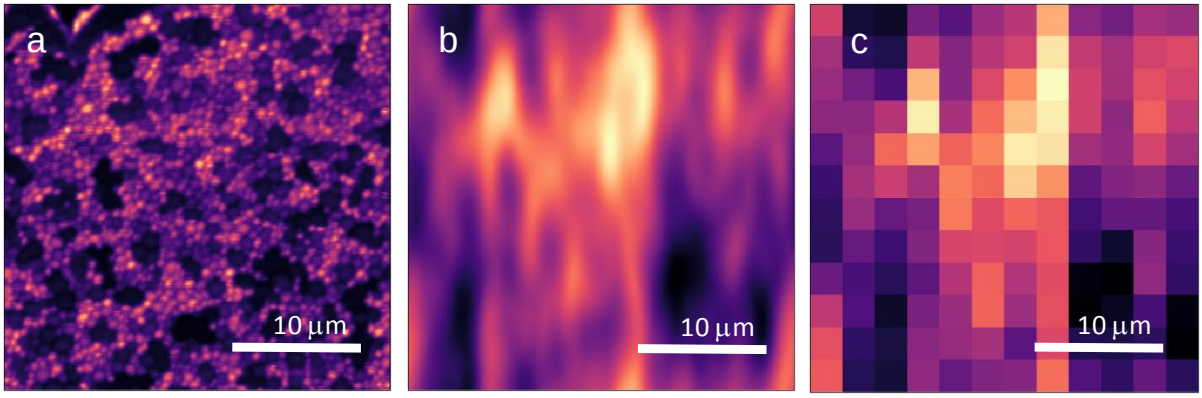

Figure S12. Confocal PL image for correlation. (a) A raw PL intensity map (b) intensity map 'blurred' at 15 ° in the Y-direction. (c) Corresponding sub-sampled pixel data to correlate micro-XRD and PL.

We now use a subsampling procedure on the blurred PL image to obtain data at the same resolution as the μXRD images. Subsampling is achieved by taking the value of the PL image in 2.5 μm steps in both x and y directions. Ambiguity exists for this procedure in the exact location of the starting position within each 2.5 μm area however, based on extensive checks, we find that the potential variation here does not significantly change our conclusions. An example of the subsampled image is shown in Figure S12c. This allows direct comparison between the PL and μXRD data. The corresponding PL decays from a weighted spatial average over the same region that the XRD beam sees when centered on the specific locations highlighted in Fig. 2a are shown in Figure S13.

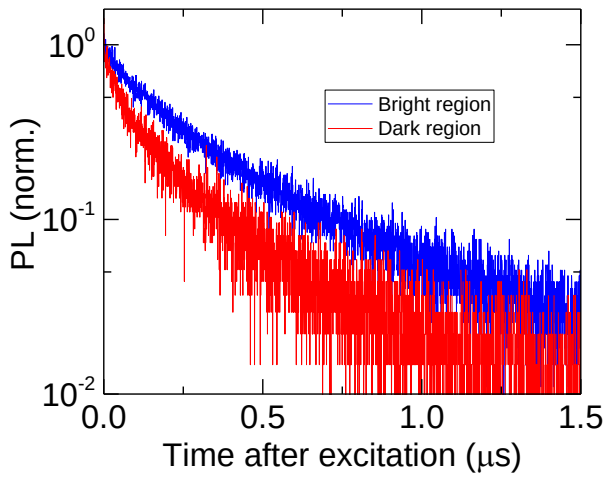

Figure S13. PL decays from a weighted spatial average over the same region that the XRD beam sees when centered on the specifics locations highlighted in Fig. 2.

Correlations between each of the datasets are assessed via linear regression. The python scipy library is leveraged to perform this regression through the function scipy.stats.linregress [8]. This function returns both an estimate of the linear fit to the data and some base statistical information about the fit including a two-sided p-value estimate based off on a t-distribution with a zero slope null hypothesis.

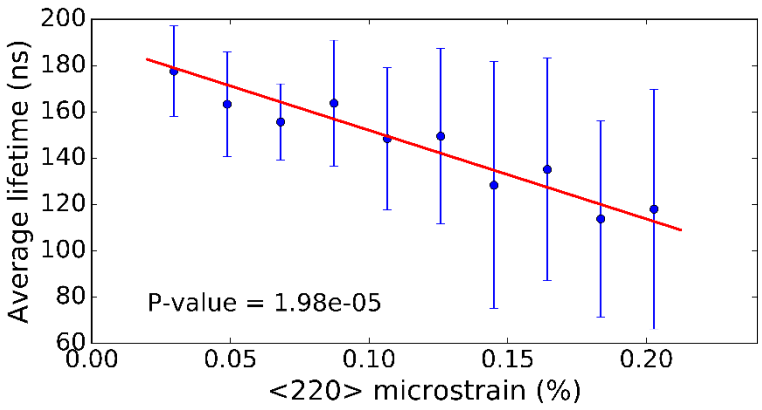

Figure S14. Statistically-significant anti-correlation of PL lifetime with microstrain of <220> reflection.

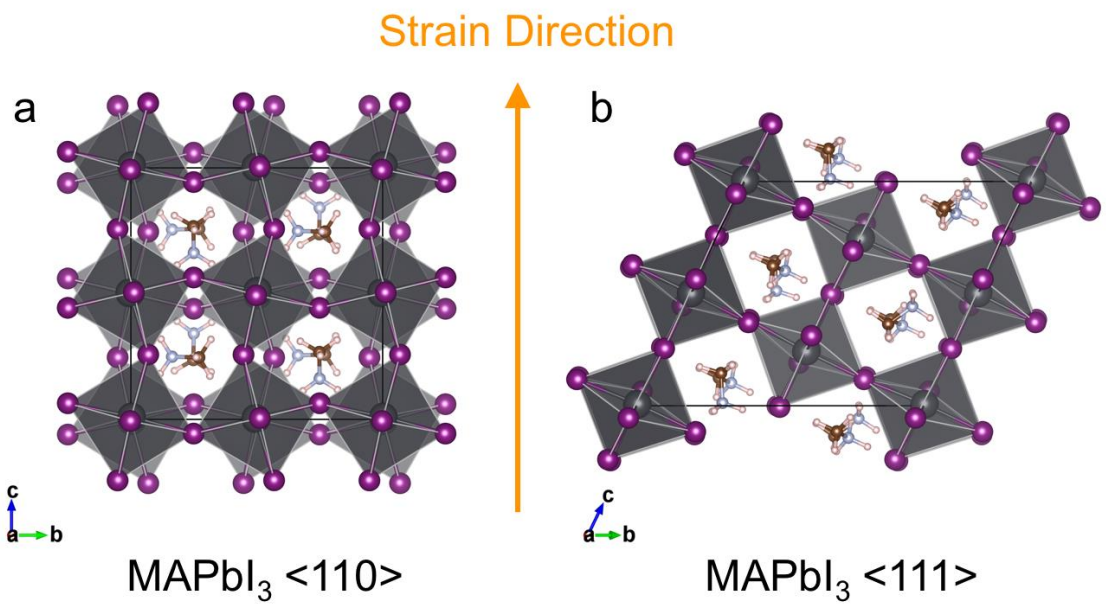

Figure S15. Atomic models which are used to simulate uniaxial strain. The both of models contain 96 atoms within the unit cell where *ab*-plane of the unit cell represents (a) <110> and (b) <111> plane and strain is applied along perpendicular direction (orange arrow) to the *ab*-plane.

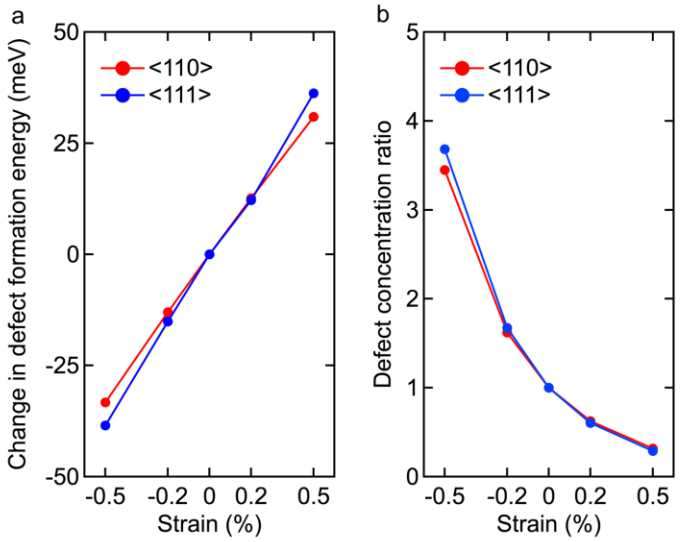

c

Strain (%)	$\Delta E_{D,\varepsilon}$ <110> (meV)	$\Delta E_{D,\varepsilon}$ <111> (meV)	$n_{D,\varepsilon}/n_D$ <110>	$n_{D,\varepsilon}/n_D$ <111>
-0.5	-33.3	-38.5	3.45	3.68
-0.2	-13.0	-15.1	1.62	1.67
0	0	0	1	1
0.2	12.6	12.2	0.63	0.60
0.5	30.9	36.2	0.32	0.29

Figure S16. (a) Change in formation energy and (b) ratio in concentration of V_I^+defects in <110> and <111> strained perovskite crystals to unstrained crystal, calculated from first-principles (T = 300 K for the defect concentration). (c) Table of the values used to plot (a) and (b).

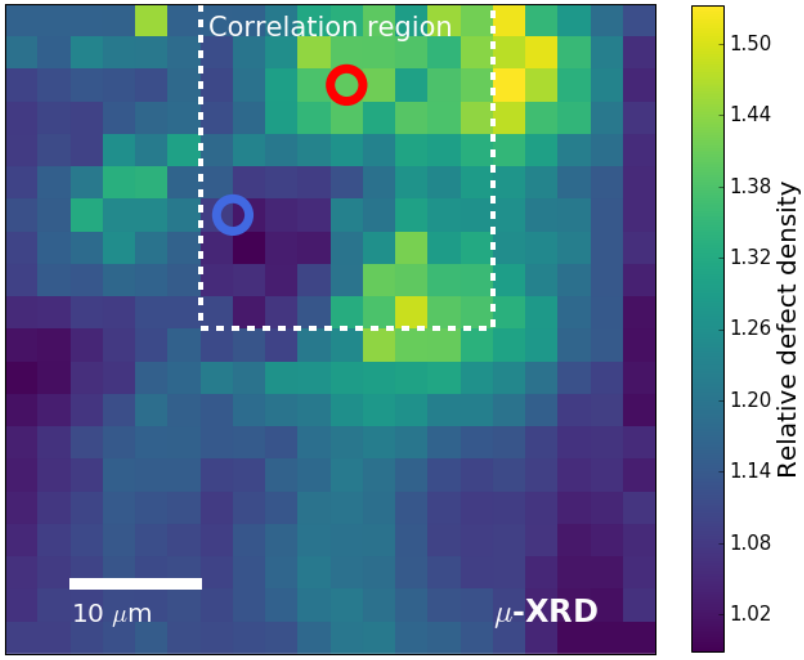

Figure S17. Spatial map of the ratio in concentration of charged iodide vacancies (V_I^+ defects) in <110> strained perovskite crystals to an unstrained crystal (calculated relationship shown in panel Figure 2e). The dashed line denotes the correlation region between μXRD and PL.

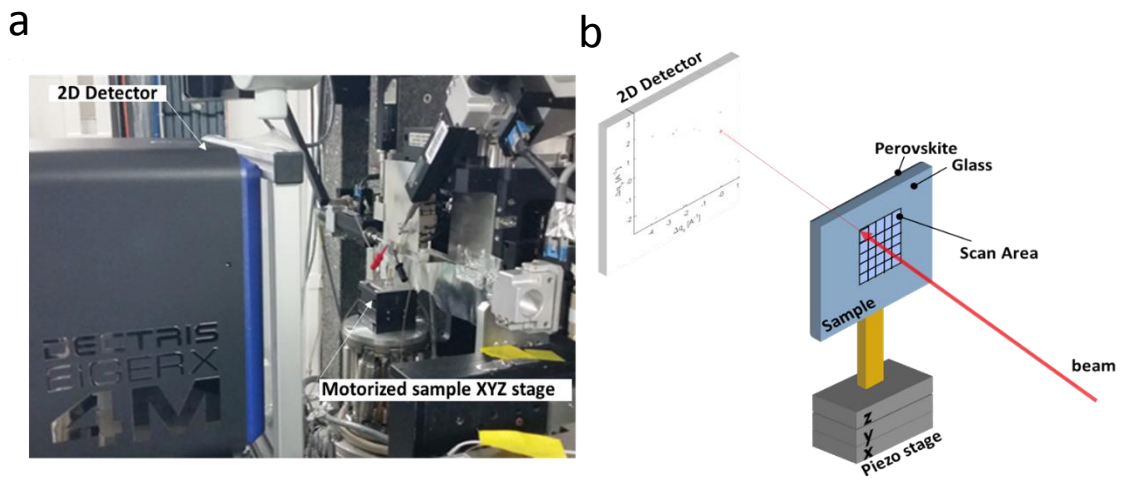

Figure S18. Overview of the nanofocus XRD setup at the ID13 beamline (ESRF). (a) Picture of the setup showing the Dectris Eiger 4M detector used to collect data and the motorized stage, where samples were mounted. (b) Diagram of the transmission geometry employed to raster scan samples.

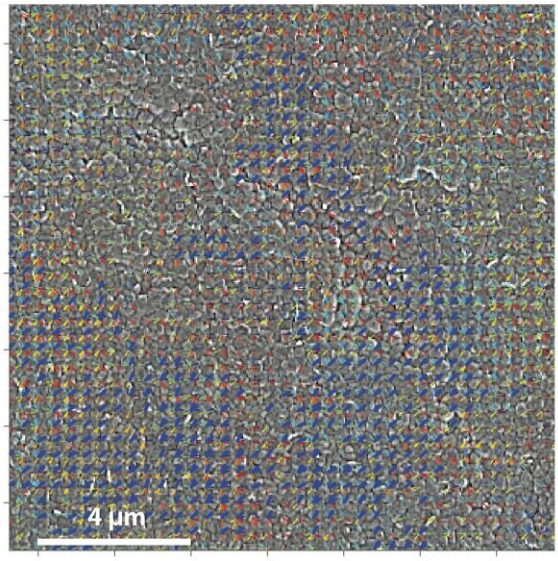

Figure S19. Overlay between the quiver plot (<210>) and SEM scan in the same scan area for a $MA_{0.15}FA_{0.79}Cs_{0.06}Pb(I_{0.85}Br_{0.15})_3$ sample showing multiple super-grains, with the largest supergrain highlighted in bold blue (cf. Figure 3e).

Supplementary References

1. Guo Z, Zhang Y, DuanMu Y, Xu L, Xie S, Gu N. Facile synthesis of micrometer-sized gold nanoplates through an aniline-assisted route in ethylene glycol solution. *Colloids and Surfaces A: Physicochemical and Engineering Aspects* 2006, **278,** 33-38.
2. Williamson GK, Hall WH. X-ray line broadening from filed aluminum and wolfram. *Acta Metall* 1953, **1,** 22-31.
3. Rivnay J, Noriega R, Kline RJ, Salleo A, Toney MF. Quantitative analysis of lattice disorder and crystallite size in organic semiconductor thin films. *Physical Review B* 2011, **84,** 045203.
4. Dollase W. Correction of intensities for preferred orientation in powder diffractometry: application of the March model. *Journal of Applied Crystallography* 1986, **19,** 267-272.
5. Wang JT-W, Wang Z, Pathak S, Zhang W, deQuilettes DW, Wisnivesky-Rocca-Rivarola F, *et al.* Efficient perovskite solar cells by metal ion doping. *Energy & Environmental Science* 2016, **9,** 2892-2901.
6. McMeekin DP, Wang Z, Rehman W, Pulvirenti F, Patel JB, Noel NK, *et al.* Crystallization Kinetics and Morphology Control of Formamidinium-Cesium Mixed-Cation Lead Mixed-Halide Perovskite via Tunability of the Colloidal Precursor Solution. *Adv Mater* 2017**,** 1607039.
7. Kunz M, Tamura N, Chen K, MacDowell AA, Celestre RS, Church MM, *et al.* A dedicated superbend x-ray microdiffraction beamline for materials, geo-, and environmental sciences at the advanced light source. *Review of Scientific Instruments* 2009, **80,** 035108.
8. scipy.stats.linregress. [cited]Available from: https://docs.scipy.org/doc/scipy-0.17.1/reference/generated/scipy.stats.linregress.html